Optomechanics for a four-stage hybrid-self-electro-optic-device-based free-space optical backplane

G. C. Boisset, M. H. Ayliffe, B. Robertson, R. Iyer, Y. S. Liu, D. V. Plant, D. J. Goodwill, D. Kabal, and D. Pavlasek

We present the design, fabrication, and testing of optomechanics for a free-space optical backplane mounted in a standard 6U VME backplane chassis. The optomechanics implement an optical interconnect consisting of lenslet-to-lenslet, as well as conventional lens-to-lens, links. Mechanical, optical, electrical, thermal, material, and fabrication constraints are studied. Design trade-offs that affect system scalability and ease of assembly are put forward and analyzed. Novel mounting techniques such as a thermal-loaded interference-fitted lens-mounting technique are presented and discussed. Diagnostic tools are developed to quantify the performance of the optomechanics, and experimental results are given and analyzed. © 1997 Optical Society of America

Key words: Optomechanics, diagnostics, alignment, optical backplane.

1. Introduction

Optical interconnects promise to alleviate the transmission bottlenecks that will appear in future computing systems as the demand for information throughput between processing elements reaches ever higher.[1] A major factor impeding progress in the field of optical interconnects is that of optomechanical constraints. Real systems will have to be designed to withstand the rigors of industrial settings if optical interconnects are ever to leave the research laboratory. Although the field of optomechanics and optical packaging has been studied for centuries[2] and is by now a well-established field with excellent references,[3–7] the field of optomechanics as applied to free-space digital optical systems is relatively new. The novel aspect of the optomechanics in this application is that the optics are used mainly to image large two-dimensional (2-D) arrays of beams. Several sophisticated digital free-space optical interconnect demonstrators have been described in the past,[8–11] along with optomechanics in such demonstrators.[12–15]

This paper analyzes the optomechanics of a four-stage hybrid bulk-lenslet free-space optical backplane demonstrator system nearing completion. The system is implemented in a unidirectional ring and comprises the optical interconnection of four hybrid-self-electro-optic device (-SEED) smart-pixel arrays. A hybrid combination of microchannel relays and conventional (bulk) relay lenses was used to interconnect the smart-pixel arrays. This system built on the previous demonstrator systems referenced above and introduces several new features, such as vertical mounting of the baseplate and installation of the system in a standard backplane chassis.

Additionally, a realistic system must remain operational even if roughly handled, and most electronic-computing systems today are exposed to mechanical vibrations originating from sources such as cooling fans blowing air over components; as the power consumption of components increases in future systems, these cooling considerations will become ever more important. As a result, future free-space optical interconnects will have to maintain their alignment and function in such a vibratory environment if they are to gain widespread acceptance. Moreover, diagnostic tools to quantify the optical misalignments, if any, caused by shock and vibrations will have to be devel-

G. C. Boisset, M. H. Ayliffe, B. Robertson, R. Iyer, Y. S. Liu, D. V. Plant, D. Kabal, and D. Pavlasek are with the Department of Electrical Engineering, McGill University, 3480 University Street, Montréal, Québec H3A 2A7, Canada. When this research was performed, D. J. Goodwill was with the Department of Electrical and Computer Engineering, University of Colorado, Boulder, Colorado; he is now with the Department of Interconnect Technology, Nortel, P.O. Box 3511, Station C, Ottawa, Ontario K1Y 4H7, Canada.

Received 11 December 1996; revised manuscript received 6 May 1997.
0003-6935/97/297341-18$10.00/0

oped. This paper also describes the design and implementation of an optomechanics diagnostic system.

The paper is structured as follows: In Section 2 we give an overview of key system aspects. In Section 3 we examine the bulk relay and the baseplate; in Section 4 we describe other modules. In Section 5 we explore the key issue of interfacing optoelectronics to optomechanics by use of a daughterboard. In Section 6 we describe a setup used to measure the performance of the daughterboard mounting technique. In Section 7 we give experimental results and follow it with a conclusion.

2. System Overview

The optical backplane was designed to implement a ring optical interconnection of four optoelectronic chips,[16] with each chip having 16 channels modulated at a maximum rate of 50 MHz. As a result, the peak theoretical bisection bandwidth of this demonstrator system was approximately 1.6 Gbits/s, which is comparable with middle-of-the-line backplanes available today.[17]

The principal optical-packaging and optomechanical objective was to interconnect optically four printed circuit boards within a standard 482.6-mm (19-in.) 6U VME[17] commercial backplane chassis. Fitting the system into the 6U chassis was a self-imposed design guideline to make the system mechanically compatible with many systems found in the field today.

An objective was also to separate the optics from the electronics so that, eventually, a user inserting a 6U circuit board into the backplane would see a conventional VME backplane environment—from a mechanical and electrical dc power perspective—while accessing the tremendous bandwidth offered by the free-space optical interconnect. In our system, this was accomplished by use of daughterboards and motherboards. The hybrid-SEED optoelectronic chips[16] were glued and wire bonded to the daughterboards residing in the optical layer; the daughterboards were then linked to the motherboards by means of a short, impedance-matched high-speed ribbon cable. As has been demonstrated previously,[18] this technique for in-

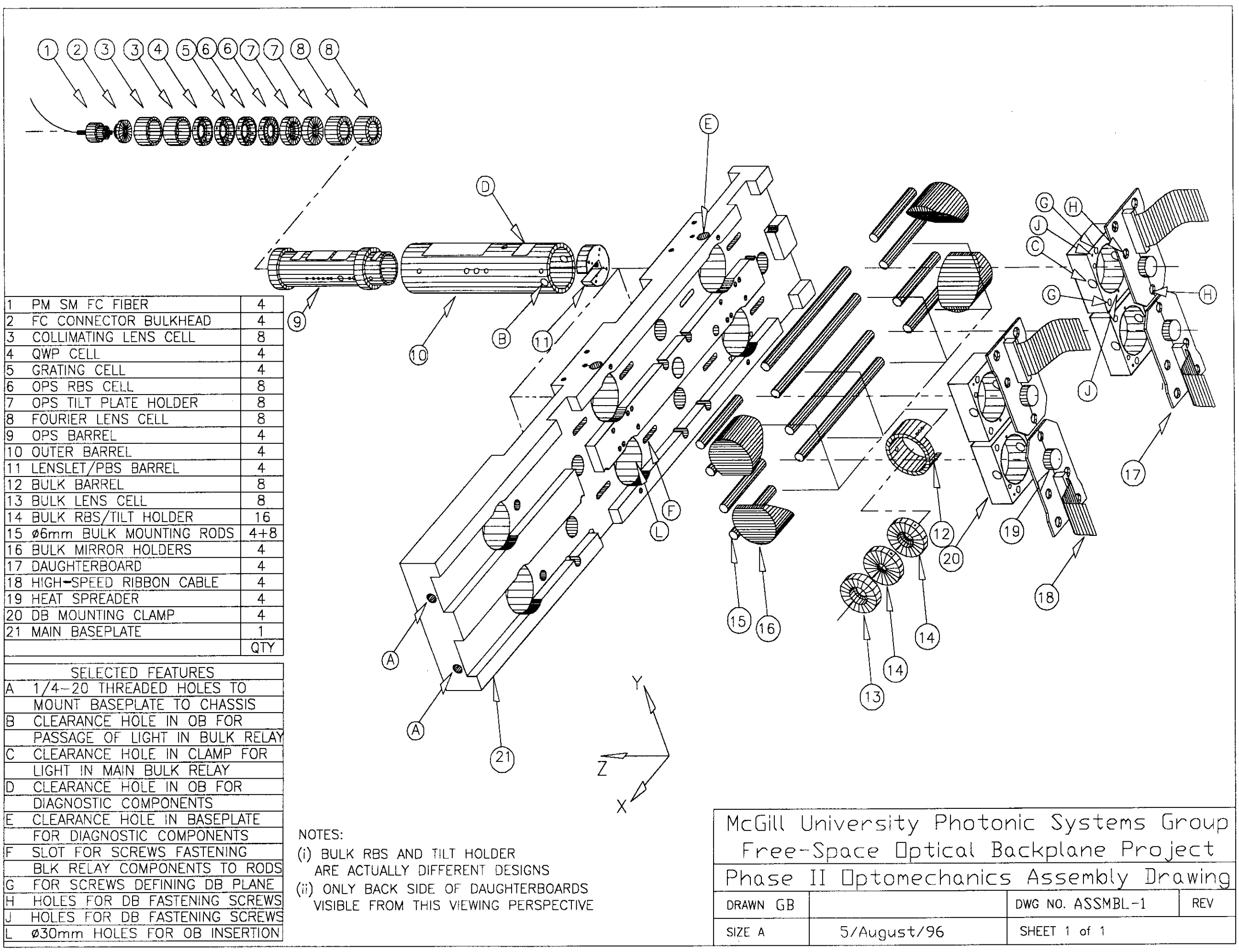

Fig. 1. Simplified 3-D system-assembly drawing. PM, polarization maintaining; SM, single mode; FC, fiber connected, QWP, quarter-wave plate; OPS, optical power supply; RBS, Risley beam steerer; PBS, polarizing beam splitter; ∅, diameter; DB, daughterboard; MB, motherboard; OB, outer barrel; BLK, bulk.

jecting electrical data from the motherboard into the optical backplane allowed for mechanical decoupling between daughterboard and motherboard while maintaining full electrical integrity between the two, provided the cable was short enough: An 8-cm length (~3-in.) was sufficient for the expected 50-MHz maximum clock speed, according to commonly used criteria for transmission-line integrity.[19]

System scalability was also a key goal. The demonstrated system occupied approximately the top half of the 6U chassis (which could therefore allow an identical system to occupy the bottom half) and featured expansion slots for interconnection of more boards if so desired. A simplified assembly drawing of the system is shown in Fig. 1. The system optomechanics had to accomplish the following tasks: (1) mechanically support the optics while respecting all tolerances demanded by the optical design, (2) support the packaged optoelectronics and interface them to the rest of the interconnect, (3) act as an interface between a commercially available electronic chassis and the rest of the system, and (4) integrate diagnostic optics and electronics for alignment and system characterization. The system as a whole had to be rugged, scalable, and easily assembled. The optomechanics were modularized as much as possible to facilitate assembly and alignment.

A key feature of this system was its three-dimensional (3-D) nature; to facilitate the discussions in this paper, it is necessary to define a frame of reference, which is shown at the bottom of Fig. 1. As can be seen, in this system the main relays that are based on bulk (conventional) optics and that implement the optical ring were in an x–y plane. However, the optical power supplies (OPS's), which illuminate the modulator chips with an array of cw power beams, as well as other relays such as the microchannels, were parallel to the z axis. Rotational directions are also defined. For example, θ_y is the angle of rotation about the y axis. Figure 2 shows a picture of the system.

A brief overview of the optical layout is now presented. Figure 3 shows an unfolded view of the overall four-stage system with one of the four OPS modules explicitly drawn. This unfolded view of the 3-D system is slightly misleading since the OPS's should actually be coming into the plane of the paper and the daughterboards should be parallel to the plane of the paper, not perpendicular, as is implied in the unfolded view.

A close-up of a hybrid stage-to-stage relay is shown in Fig. 4. Gaussian beam-propagation models were used in the design of the system. At each stage, lenslets were close to the smart-pixel devices to be able to collect the beams and reduce their numerical aperture, and bulk (conventional) lenses[20] relayed the beamlets from one stage to another. The lenslets reduced the numerical aperture of the beams relayed by the bulk lenses to less than 0.025. All lenslets were 125 μm $\times$ 125 μm eight-level diffractive structures with a focal length of $f_\mu = 768\ \mu m\ at\ \lambda =$ 850 nm. Lenslet array 1 (LA_1) consisted of alternat-

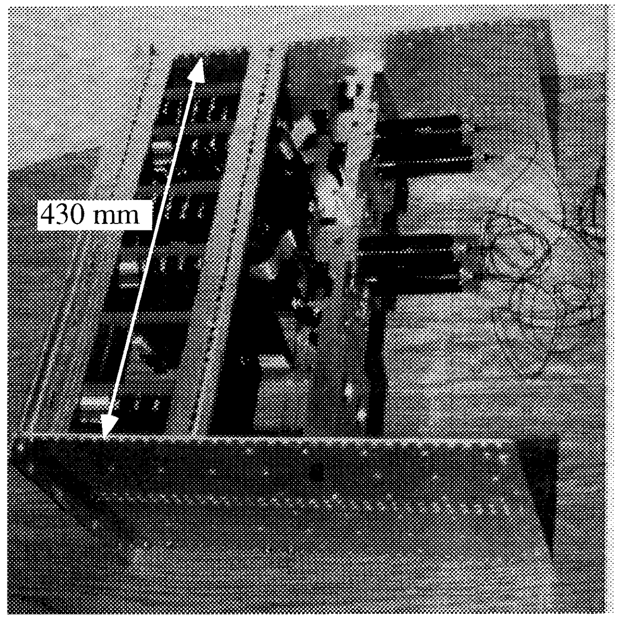

Fig. 2. Photograph of the system mounted in a standard 431-mm-wide (17-in.-wide) 6U VME chassis.

ing 1 $\times$ 8 lenslet strips and pixellated mirror strips 123 μm wide $\times$ 1 mm high. Lenslet array 2 (LA_2) consisted of an 8 $\times$ 8 array of lenslets. These are shown in Fig. 5. Additionally, alignment features were placed around the peripheries of the arrays.

The fiber-connected OPS generated an 8 $\times$ 4 array of right-hand circularly polarized cw beamlets at the power-array plane that was relayed by LA_1 and LA_2 to the smart pixel. The beamlets were then modulated by the chip, relayed through LA_2, and imaged by the bulk relay to stage 2. At stage 2, the beamlets were reflected by the polarizing beam splitter (PBS), then reflected off the pixellated mirror on LA_1, and finally imaged onto the receiver on board 2 by means of LA_2. The polarization components, namely the quarter-wave plates (QWP's) and the PBS were used for beam combinations, as discussed in Ref. 21. The optical microlens relay was designed to relay the beams using the maximum lens-to-waist configuration.[22] Tilt plates and Risley beam steerers (RBS's) were included for alignment purposes. The dimension of the array of beamlets was nominally 1.2 mm $\times$ 1.2 mm.

Space constraints were such that the aperture stop for the bulk interconnect lay between the PBS–QWP assembly and the RBS's at the entrance to the lenslet barrel (described below). This stop was 4.10 mm in diameter. To a first order this left an ~500-μm clearance between the edge of the outermost beamlet and the stop. As a result, any offset greater than 500 μm on the bulk interconnect would lead to considerable clipping of the outermost beamlet. However, as we show below, the alignment budget permitted only a smaller misalignment of 220 μm at the pixellated mirrors, since this was the maximum travel of the tilt plates.

This paper does not present a detailed analysis of the optical system. However, there were several crit-

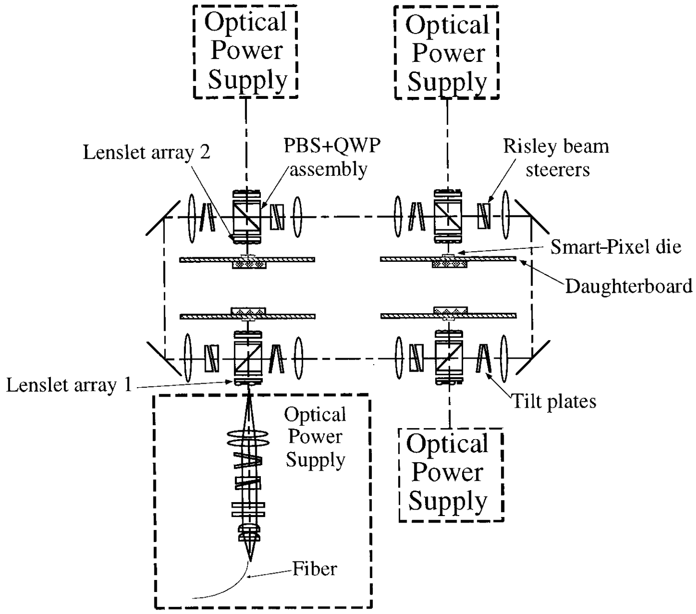

Fig. 3. Unfolded system optical layout.

ical and extremely tight optomechanical-alignment tolerances that influenced much of the design and must be given here. These tight tolerances were driven by the extremely small size of the multiple-quantum-well windows that all beams had to hit. The multiple-quantum-well windows were 20 μm × 20 μm (Ref. 16), and the beams incident on them had a nominal diameter (99% encircled power) of 19.5 μm. This situation imposed extremely tight tolerances, which are given in Table 1. Among other tolerances given, Table 1 indicates that the lateral-alignment (*x–y*) error between the microlens array and the smart-pixel device array had to be <1 μm to keep losses from misalignment to less than 1% optical power. Other demanding tolerances were the lenslet-to-lenslet alignment tolerances, key values of which are given in Table 2. As can be seen, the bulk interconnect tolerances (~220 μm) were much looser than the lenslet-device tolerances (~1 μm) or the lenslet-to-lenslet tolerances (~5 μm).

3. Baseplate and Bulk Relay

A. Baseplate Description

The baseplate was the central piece of the optomechanics and acted as the support structure for the entire optical–optomechanical layer. All other optomechanical and optical components were either attached to the baseplate or locked into barrels attached to the baseplate. The baseplate, a simplified sche-

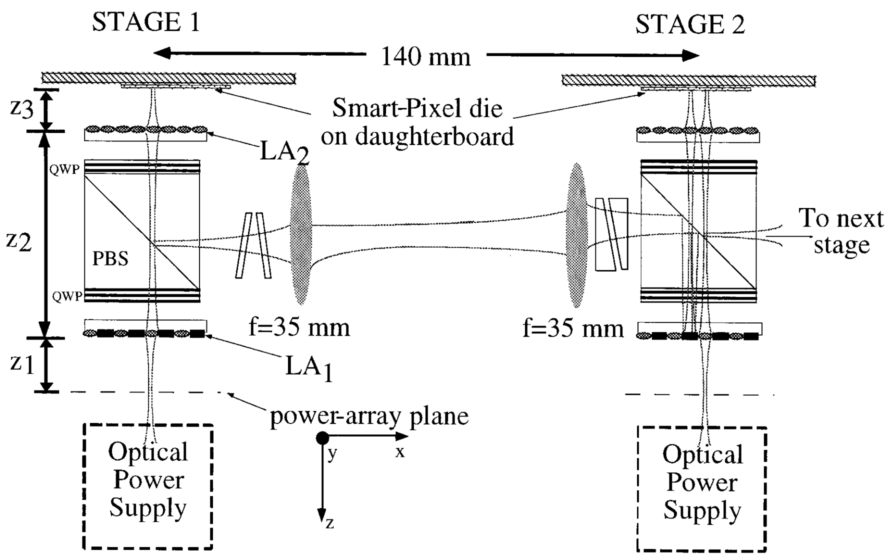

Fig. 4. Close-up of one board-to-board relay.

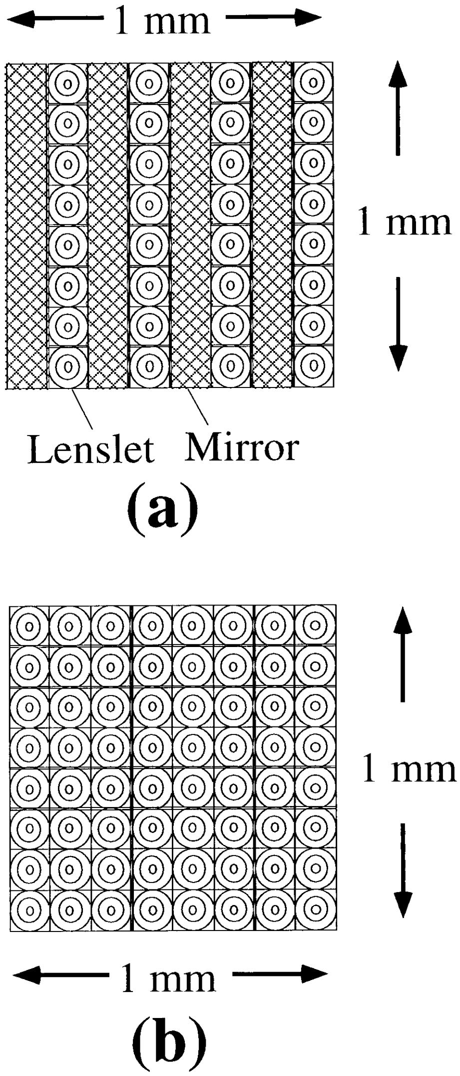

Fig. 5. Lenslet-array schematics: (a) lenslet array 1 (LA_1) and (b) lenslet array 2 (LA_2).

matic of which is shown in Fig. 6, was 431.8 mm (17 in.) long (the inside of the standard VME rack is 50.8 mm shorter than the outside because of mounting flanges), was mounted vertically into the chassis, and was bolted to the side panels of the chassis.

Previous free-space optical-switching demonstrator systems used aluminum or steel for baseplates, but it was determined that neither of these materials was suitable for production.[12] The baseplate for this system was made of magnesium AZ31B; the main reasons for choosing this metal were its ease of machinability, its lightness, and its low residual stress, which minimizes the need for stress relief when compared with other metals.[23] This type of metal has already been used in applications such as lens mounting.[24] Note that magnesium is softer than other frequently used materials: The Brinell hardness number (BHN) of magnesium is 82, compared with 95 for aluminum 6061-T6 or ~200 for 1080 steel (depending on drawing and other processes). This softness makes magnesium easier to machine but more easily dented,[25,26] which prompted the use of rods for

Table 1. Daughterboard Alignment Tolerances[a]

Degree of Freedom	Board Position and Tolerance to be Met	Board Position before Gluing	Board Position after Gluing
Δx (μm)	0 ± 1	0 ± 2	3.2 ± 3
Δy (μm)	0 ± 1	0 ± 2	-2 ± 3
z_3 (μm)	886 ± 15	887 ± 15	875 ± 15
Tilt θ_x	$0° \pm 0.5°$	$0.06° \pm 0.1°$	$0.55° \pm 0.27°$
Tilt θ_y	$0° \pm 0.5°$	$0.04° \pm 0.1°$	$0.18° \pm 0.14°$

[a]Tolerances for positioning of the smart-pixel die on the daughterboard with respect to the optics. For each degree of freedom, columns 2–4 indicate (a) the positioning objective to be met for a <1% loss, (b) the measurement when the board is held at its nominal position by the positioning stage and is about to be glued to the optomechanics, and (c) the final position after the daughterboard is glued to the optomechanics and the stage is removed, respectively. The parameters Δx and Δy were measured 9 weeks after gluing; the other parameters were measured 4 days after gluing.

mounting the bulk optics (described in Subsection 3.C.2).

The main outer barrels, each one containing an OPS and a microlens relay, fit into the holes labeled L in Fig. 6, which were 30 mm in diameter. Of these six holes, four were used in the actual system (those at $x = 75$ mm and $x = 215$ mm); two others (at $x = 355$ mm) were kept for future system expansion.

Many holes and slots were included for diagnostic, assembly, and alignment purposes. Additionally, magnets were glued into holes machined at the back of the baseplate. They served to keep the bulk-mounting rods (described below) in place on the vertical baseplate during assembly, until the bulk components were bolted onto the rods.

B. Baseplate Machining and Characterization

Machining of the baseplate was performed as follows: The magnesium plate from which the baseplate was machined was clamped to the apron of a DRC 600 (Bridgeport) milling machine, and three 9-mm-deep main cuts in the y direction were made; these are the cuts that most affect baseplate bowing in θ_y. Most of the smaller clearance slots for the bulk-barrel screws were also machined at this time. A fly-cutter finish (with the cutter turning at 1200 rpm, a feed rate of 152 mm/min, and a cut depth of 125 μm) ensured a smooth surface for subsequent flatness measurements.

The flatness of the baseplate was measured in the main slots (in the x direction) along the two lines AA′ and CC′, as shown in Fig. 6. For performing these measurements, the baseplate rested on a granite

Table 2. Lenslet Alignment Tolerances[a]

Degree of Freedom	Position and Tolerance to be Met
LA_1 to LA_2 (x, y)	0 ± 5 μm
z_1	922 ± 15 μm
z_2	6.981 ± 0.15 mm

[a]Tolerances for lenslet-to-lenslet alignment as imposed by the optical design; z_1 and z_2 are as defined in Fig. 4.

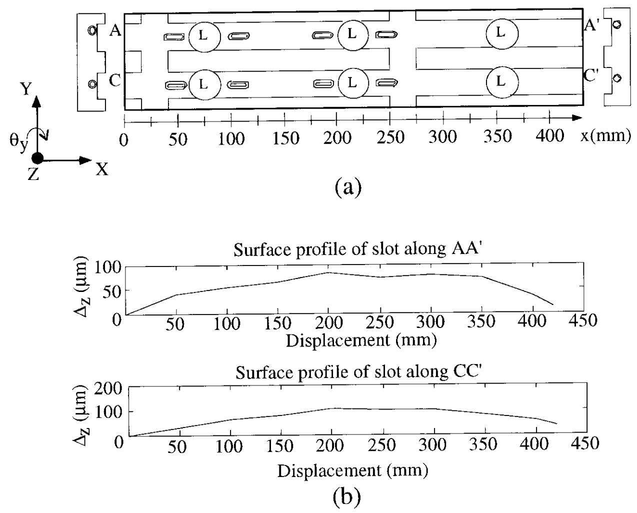

Fig. 6. (a) Sketch of the baseplate. (b) Surface profile of the baseplate along the slots.

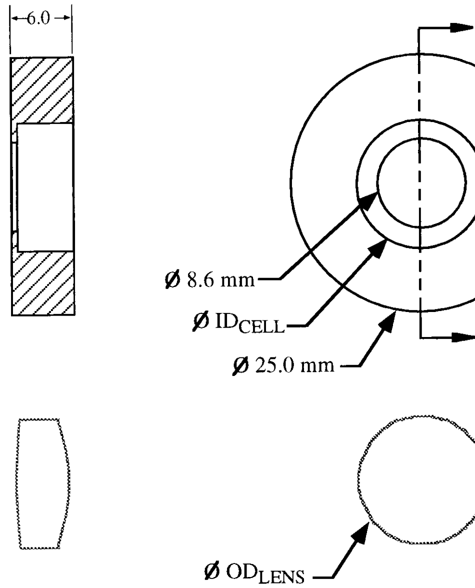

Fig. 7. Bulk lens and holder used for the FN1 interference-fitted lens holder. For an interference fit, $OD_{LENS} > ID_{CELL}$.

measuring slab and a level indicator was passed along the bottoms of the slots at approximately the place where the rods holding the bulk barrels made contact with the bottom of the slot. The maximum deviation was $\sim$125 μm from one end of the baseplate to the other and was considerahly less over the stretch ($\sim 50 < x < 275$ mm) where the bulk relay actually resided. The use of rods (described below) for bulk mounting further helped reduce the effect of baseplate irregularities on the optical axis by averaging out surface irregularities. The repeatability of the flatness measurements was better than 10 μm.

These flatness values were well within the overall bulk interconnect alignment tolerance budget.

C. Bulk Barrel Assembly

The bulk lenses, RBS's, and tilt plates were mounted into their respective holders. Afterwards, as can be seen from the assembly drawing (Fig. 1), the mounted bulk lens and a pair of mounted steering elements (either a pair of RBS's or a pair of tilt plates), respectively labeled components 13 and 14 in Fig. 1, were inserted into a modular bulk barrel (component 12). This bulk barrel was then bolted to the baseplate.

1. Thermal Effects in Bulk Relay Lens Inner Mounting

Although many techniques exist for mounting lenses into cells,[3] none of these techniques left enough room to fit the bulk lenses and the steering elements (either RBS's or tilt plates) between the bulk turning mirror and the daughterboard. It was thus decided to forego any retaining ring and instead hold the lenses in their cells by use of the force of an interference fit between the outer diameter of the lenses, OD_{LENS}, and the inner diameter of the cells, ID_{CELL}, as shown in Fig. 7. In other words, $OD_{LENS} - ID_{CELL} = I$, where I is a positive number called the interference. Interference fits are frequently used in industry to maintain a constant bore pressure in hole–shaft assemblies; the difference between minimum and maximum values in the machining tolerances is kept small.[25]

The OD_{LENS} of the eight bulk relay lenses in the system were measured to be between 12.468 and 12.479 mm (±2.5 μm).

The use of interference fits posed several design challenges, most of them related to thermal issues. The first challenge was assembly. To first put the lens into the cell, we found that the easiest way was to heat the cell (but not the lens) to make it expand and then to insert the lens. As the cell cooled and shrank, the lens was held snugly.

Another challenge was the choice of material. The material chosen for the cell ended up being Delrin.[27] Its main drawback, namely, a high coefficient of thermal expansion $CTE_{DEL} = 97$ parts in 10^6/°C (ppm/°C), was compensated by its low cost, immediate availability, ease of machining, and low Young's modulus (in both compression and tension) of $E_{DEL} =$ 2.76 GPa, which reduced the stress caused by thermal mismatch. In comparison, the numbers for the glass of the lens were similar to those of BK7: $CTE_{LENS} = 7.1$ ppm/°C and $E_{LENS} = 81$ GPa.

Using an interference fit with two such thermally mismatched materials can cause two main problems: (1) As the temperature T increases, the interference I decreases. Eventually, at T_{fall} the lens can simply fall out. (2) As T decreases, I increases, causing severe radial stress. This can lead to birefringence and possibly damage to the cell, the lens, or both.

Machining one different cell for each lens would have been prohibitively expensive, so one value of ID_{CELL} at 20 °C, ID_{CELL20}, was chosen for all cells. The basic criterion for computing the nominal value of ID_{CELL20}, was that, at a maximum operating temperature T_{max}, the interference should still lead to a FN1 interference fit (2.54 μm $< I <$ 20.3 μm) for all

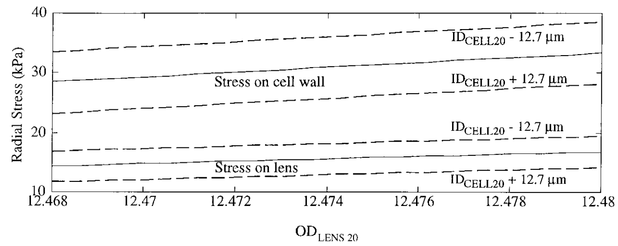

(a)

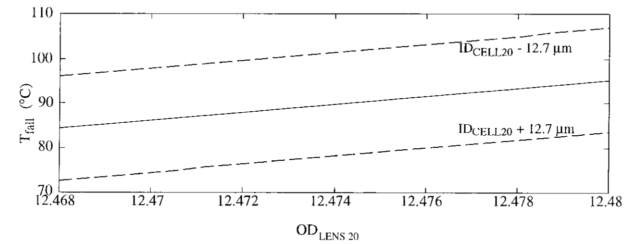

(b)

Fig. 8. (a) Curve relating the radial stress on the components to the lens outer diameter. (b) Curve relating the temperature at which the lens falls out to the lens's outer diameter.

lenses. This fit, described as a light drive fit, is used for permanent assemblies and produces a light assembly pressure.[25] The maximum operating temperature T_{max} was chosen to be 85 °C since this is the maximum tolerable case temperature for a commercial-grade Pentium Pro.[28]

The relations for calculating the radial stress in the lens, S_{RLENS}, and in the cell wall, S_{RCELL}, are[3]

$$S_{LENS} = \frac{(CTE_{DEL} - CTE_{LENS})\Delta T}{1/E_{LENS} + OD_{LENS}/(2E_{DEL}t_c)}, \quad (1)$$

$$S_{RCELL} = \frac{(OD_{LENS})(S_{RLENS})}{t_c}, \quad (2)$$

where the cell-wall thickness t_c is nominally 6.3 mm.

Given the above, ID_{CELL20} was calculated to be 12.397 mm, and Fig. 8 shows plots of the stresses on the cell and lens [Fig. 8(a)] and of T_{fall} [Fig. 8(b)] as a function of OD_{LENS}. The bands above and below each solid curve represent the effect of a machining error of ± 12.7 μm on the value of ID_{CELL20}. It can be seen that a smaller cell inner diameter leads to greater stress and a greater T_{fall}. As a result, in the worst-case combination of lens tolerances and cell inner-diameter tolerances, the interference can fall to zero and the lens can fall out of the holder at 72 °C. At the other extreme worst case, the radial stress in the cell can reach 38 kPa, which is slightly over half of the 68-kPa nominal tensile strength of Delrin.[27] In all cases, calculations[3] revealed that the stress-induced birefringence was negligible.

Experimental validation was conducted on this technique. In the first experiment, the lens was mounted by use of the technique described above in this subsection. A beam was then passed through the lens, the cell with the lens in it was rotated, and the movement of the spot caused by the focused beam was observed in the focal plane. The spot traced out a circle with a radius of 3.5 μm (± 1 μm). Since this passive-mounting technique cannot correct for defects within the lens, such as the intrinsic wedge angle or centering of the lens optical axis with respect to its mechanical axis, these have to be added to obtain a true picture of the centering accuracy. For the current lens, these additional factors could have added up to 10 μm to the radius of the circle traced out by the spot.[20] Consequently, this is a cheap and rapid technique for use only with good-quality, well-centered lenses; as a result, the technique demonstrates that the cost of lens mounting can be pushed back from the optomechanical assembler to the lens and cell fabricators.

In another experiment, a mounted lens with an outer diameter of $OD_{LENS} = 12.469$ mm at 20 °C was heated until the lens fell out. The lens did indeed fall out at $T_{fall} = 100$ °C $\pm$ 10 °C, showing that the technique worked as expected. This mounting process illustrates the compromises between ease of assembly, operating temperature, material selection, and tolerances that must be considered when designing and building optomechanical components.

2. *Bulk-Barrel Mounting*

After the bulk barrels were assembled they had to be mounted onto the baseplate in their proper positions. As with other similar systems,[8] slots were cut into the baseplate and the bulk barrels rested in these slots. However, given the vertical mounting and the rough handling the system was expected to receive in the chassis, the standard magnetic retaining techniques used in many other digital free-space optical interconnect demonstrations[8,10,11] were rejected; instead, all bulk-relay components (bulk barrels and mirrors) were bolted into the baseplate. Furthermore, the barrels were not in direct contact with the edges of the slots. Instead, hard, precision-ground stainless steel rods 6 mm in diameter were inserted into the slots and the components rested on the rods, as shown in Fig. 9. Such rods are cheap and readily available.[29] The outer-diameter tolerance of the above rods was +0 to −10 μm, and the outer diameters of the machined outer-barrel components were measured to have a deviation of ± 10 μm from their nominal 30 mm.

Machining tolerances were the most important factor affecting the height of the optical axis. Other physical parameters were nonetheless studied, as they gave insight into the design. One of these parameters was the deformation of the barrels arising from the holding force exerted by the screws. If we assume that the screw threaded into the hole in the barrel can be modeled by a nut–bolt fastening, the holding force P exerted by the screw can be estimated to be[30]

$$P = T/(KD). \quad (3)$$

For the 4-40 screw used, T is the installation torque (nominally 0.6 N · m for an 18-8 steel 4-40 screw), K is the torque coefficient (~0.15 for plated finish fas-

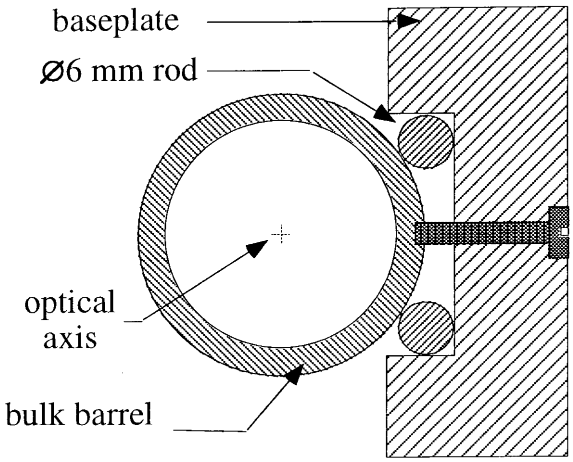

Fig. 9. Technique for mounting bulk-interconnect components onto a vertical baseplate. The bulk barrel has an inner diameter of 25 mm and an outer diameter of 30 mm.

teners), and D is the nominal screw diameter (2.79 mm for a 4-40 screw).[30] This yields $P = 1434$ N ($M = 1434$ N/9.8 = 146.3 kg).

This exerted force can damage the barrels, the rods, the baseplate, or any combination of these by causing indentations in the material. The most critical interface is between the barrel and the rods, and the damage to this interface can be estimated as follows. By use of the BHN's, the surface area A of the indentation in the barrel caused by the hard steel rods biting into the barrel can be approximated as[31]

$$A = 0.5 \times M/\mathrm{BHN}, \tag{4}$$

where the factor of 0.5 is due to the fact that each rod exerts only half the force on the barrel.

Using a value of BHN = 95 (Ref. 25) for the 6061-T6 aluminium used in the barrels means that the surface area A should be $0.5 \times 146.3/95 = 0.77$ mm^2. Further geometrical analysis indicates that, for a line contact of 13 mm (the length of the barrel) and a rod diameter of 6 mm, the drop in the height of the optical axis resulting from indentations is of the order of 1 μm, which is less than the machining error. This drop was further reduced by anodization of the barrels: Anodization increased the hardness of the barrels, thus reducing indentations in the barrels to negligible levels.

To summarize, the considerable forces involved in bolting the bulk barrels down onto the baseplate caused no significant damage to any component. It will be seen below, however, that the force involved in bolting a daughterboard to the optomechanics caused significant problems. Other forces, such as the force exerted between baseplate and rods, were spread over the length of the rods and as such could be neglected.

D. Bulk-Turning-Mirror Alignment

The optical system was a closed-loop ring system. As such, turning mirrors had to be installed at the four corners of the optical system to close this loop. Since errors in mirror alignment could be corrected only by the bulk RBS's and tilt plates, which had a wedge angle of 1° and a tilt angle of 10°, respectively, it was imperative that the mirrors be aligned as carefully as possible to reduce the travel requirements of the steering optics. Additionally, the mirrors had to be arranged so as to eliminate rotation of the 2-D array of beams.[32] In the overall system-assembly sequence, one of the first steps was mounting of the bulk turning mirrors onto the baseplate, as outlined in Fig. 10. This subsection describes the process.

Before assembly was started, all the mirrors were glued to their holders, which allowed for two degrees of freedom in tilt and rotation. Aligning the four mirrors into a loop presented a certain problem. In a system such as this, the slots in the baseplate can be used to locate the optical axis as it goes through four 90° turns in the loop. Apertures placed along the slots or along mechanical extensions of the slots can be used to define the optical axis; the further the apertures are from each other (i.e., the greater the lever arm), the better the optical axis can be defined.

It is therefore possible for one to align the mirrors by launching a reference beam that is known to be on axis and monitoring the reflected beam on an aperture far from the baseplate. However, this procedure works for only the first three mirrors; placing the fourth mirror closes the loop, and a lever arm longer than the baseplate cannot be used. For avoiding this problem, a technique involving a pellicle was used.

With no mirrors on the baseplate, a reference beam was launched down the barrel of the pellicle holder, at the end of which was fixed a 70/30 (transmissive–reflective) pellicle, as shown in Fig. 10. Seventy percent of the beam went through (beam T), and 30% was reflected toward position 1. Using customized alignment apertures on the baseplate and along the optical bench allowed the pellicle holder and incoming beam to be adjusted until they delivered a beam that was coaxial with the optical axis on the baseplate. The beam was parallel to the ideal bulk optical axis to within a few minutes and was less than 50 μm off axis. Afterward, bulk turning mirror 1, in its holder, was installed. After adjusting the mirror so that the reflected optical beam going toward position 2 was again parallel to and on the axis, mirror holder 1 was bolted. This procedure was repeated for mirrors 2 and 3. For the final mirror holder (4), the reflected beam R_1 was observed and the mirror holder was adjusted so as to minimize the angle β; mirror holder 4 was then bolted. The pellicle thus brought the reference beam off the baseplate and allowed for a lever arm to improve the accuracy of the alignment.

Figure 11(a) shows spots resulting from beams T, $R_1, R_2, R_3, \ldots$, which are projected onto a screen 3 m from the baseplate. This large (3-m) distance allows a lever effect to magnify the error in β. To obtain this picture, mirror 4 was deliberately misaligned; the actual alignment, which was much tighter ($\beta < 0.05°$), was similar to that shown in Fig. 11(b). This misalignment was sufficiently small for eventual correction by the bulk RBS's and tilt plates.

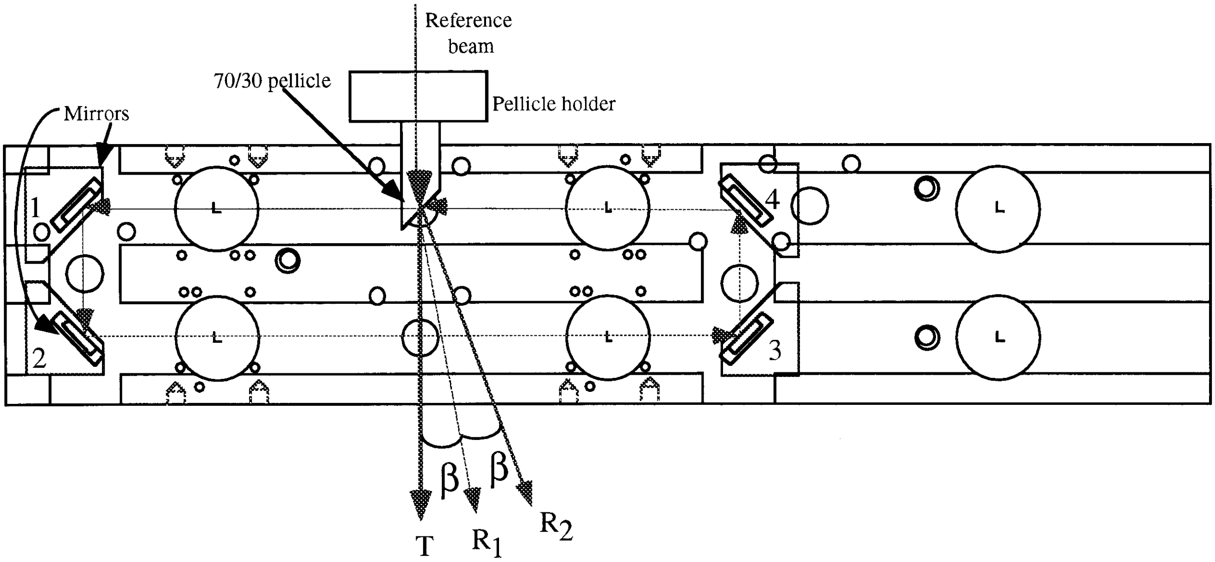

Fig. 10. Setup for mounting and aligning bulk turning mirrors on the baseplate.

4. Other Modules

This section covers the optomechanics associated with other key modules. It concludes with a first-order alignment-tolerancing analysis.

A. Lenslet–Beam-Splitter Barrel

A simplified drawing of the lenslet–beam-splitter barrel is shown in Fig. 12(a). To assemble the unit, we first aligned the PBS with the QWP's mounted on it (PBS–QWP) and then glued it inside the slot, as shown in Fig. 12(b). With a customized setup, the PBS was glued with an angular error of $\theta_y < 0.05°$. The lenslets were then glued to the faces of the barrel, as shown in Figure 12(c).

We met the demanding lenslet-to-lenslet alignment tolerances in (x, y) listed in Table 2 by building a separate prealignment and imaging rig. The tolerances in the spacing ($z_2 = 6.98$ mm; Fig. 4) between the lenslet arrays, as well as the relative tilt (θ_x and θ_y) between the lenslet arrays, were dictated by the machining tolerances, which were ± 10 μm for this case. These tolerances were well within those demanded by the optical design. When the lenslet–beam-splitter barrel assembly was complete it was inserted into the outer barrel; these components are pieces 11 and 10 respectively, in Fig. 1.

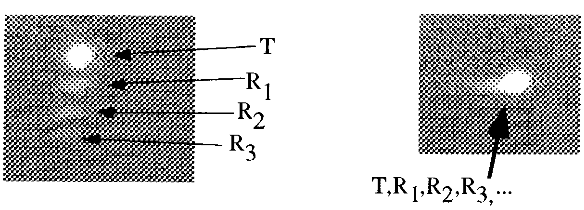

(a) (b)

Fig. 11. Results of the alignment of the bulk turning mirror: (a) mirror 4 greatly misaligned and (b) mirror 4 at its optimum alignment.

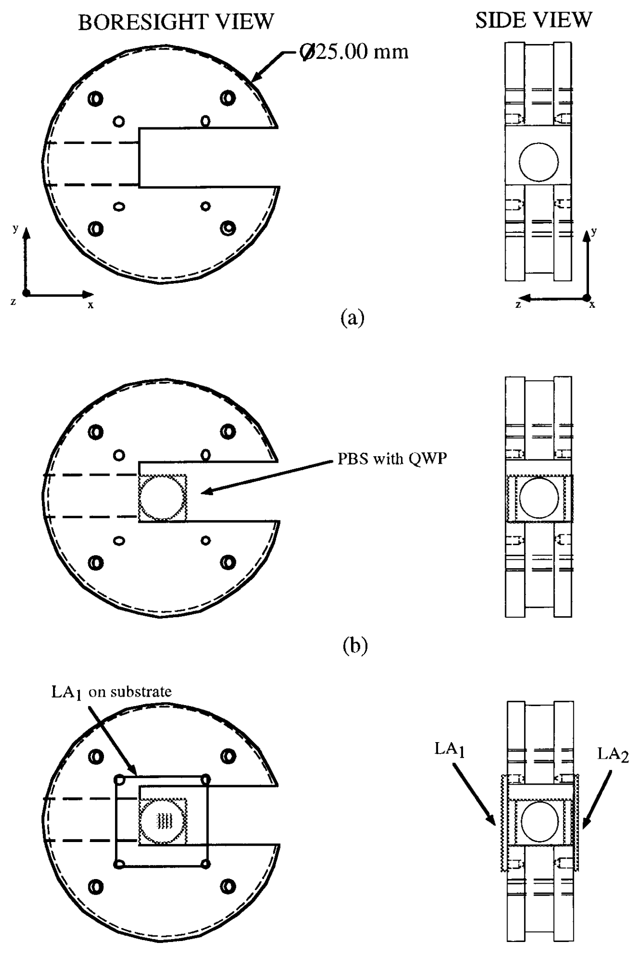

(a)

(b)

(c)

Fig. 12. (a) Lenslet–PBS barrel. (b) Lenslet–PBS barrel with the PBS mounted. (c) Lenslet–PBS barrel with the lenslets mounted.

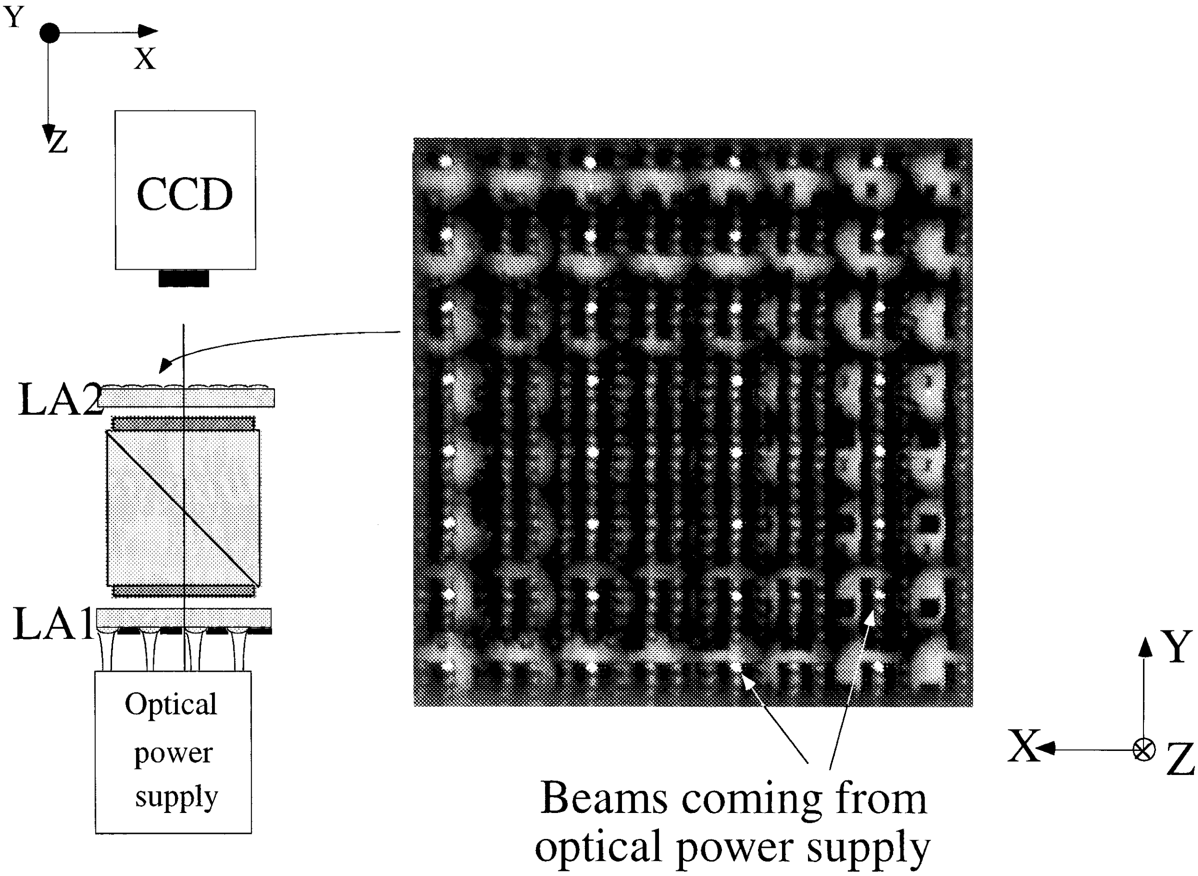

Fig. 13. LA_1 imaged by LA_2.

The optical microlens relay, which was designed to relay the beams by use of the maximum lens-to-waist configuration,[22] also exhibited another interesting characteristic: If we let z_2' (=5.41 mm) be the optical distance between actual LA_1 and LA_2 and z_3 (=886 μm) be the optical distance from LA_2 to the device plane, then $1/z_2' + 1/z_3 \approx 1/f_\mu$. As a result, each lenslet on LA_2 imaged a part of substrate 1 and relayed it to the device plane. These relayed images, with backillumination shown in Fig. 13, clearly indicate the strips of pixellated mirrors and lenslets on LA_1. In addition, the beamlets from the power-array plane clearly appear as bright spots coming from the lenslets. This qualitatively demonstrated that the lenslets were properly aligned and was of great help during system alignment.

B. Optical Power Supply

The OPS contained lenses to collimate the output from the fiber, a multiple-phase grating as a fan-out element, a Fourier transform lens pair, and additional components for beam-steering and polarization control. Each OPS barrel was 80 mm long. Each fully assembled OPS was prealigned separately and inserted into an outer-barrel assembly (components 8 and 10 in Fig. 1). At the end of this assembly sequence, therefore, each outer-barrel assembly contained a lenslet–beam-splitter barrel and an OPS. The outer barrels were then inserted into the baseplate. A full analysis of the OPS performance is the subject of another paper.[33]

C. Bulk-Interconnect Tolerancing

As shown in Fig. 4, the bulk interconnect had to relay the beams emerging from stage 1 onto the pixellated mirror of stage 2. The two bulk tilt plates, each 1.5-mm-thick SF10 (n = 11.71) glass at a 10° tilt, could each move the beam array approximately 110 μm at the pixellated mirror. By rotation of the tilt plates such that their individual contributions cancelled, it was possible to move the imaged beam array by 0 μm at the mirror plane; conversely, they could also be oriented such that they gave a total displacement of 220 μm at the pixellated mirror.

An ideal system would require no correction that was due to misalignment. In the present nonideal case, the following factors—mentioned in Section 4 above—contributed to misalignment, which had to be corrected by the tilt plates: machining errors affecting the outer diameter of the bulk barrels and the depth and width of the baseplate slots (~25 μm), the lens-centering error (~10 μm), rod deformation (~10 μm), baseplate-bow errors (~50 μm) from inserting the beam splitters into the outer barrels (~50 μm, total), and alignment errors in the bulk mirrors (~50 μm). To a first-order approximation, these errors could have caused a total alignment error of 90 μm (in quadrature addition) in addition to aberrations. This alignment error is corrected easily by the tilt plates.

5. Daughterboard Mounting Techniques

Mounting the daughterboards to the optomechanics was the most critical step of assembly since it involved interfacing the optoelectronics to the optomechanics. This section describes the various techniques implemented and the challenges that had to be overcome.

A. Procedure

This operation, which was performed four times, once for each daughterboard, was the most delicate of the entire assembly. The key components are outlined in Figs. 14(a) and 14(b) in a rear view and side view, respectively. In short, the daughterboard was attached to an interface piece called the daughterboard clamp, which was bolted to the baseplate.

The optical design specified that the smart-pixel device plane be $z_3 = 886 \pm 15$ μm away from the microlens array and that the x–y alignment error between lenslets and smart-pixel device windows be of the order of 1 μm, as shown in Table 1. These very tight alignment tolerances were required to reduce the loss of optical throughput resulting from daughterboard misalignment to below 1%. Misalignments greater than those given in Table 1 will cause a loss greater than 1%.

Since there were very few optoelectronic chips or lenslets available, it was decided that the step of gluing LA_2 to the device packaging would not be performed. Rather, a four-step assembly sequence was implemented. With the daughterboard mounting clamp already bolted to the baseplate, the objective was to align the daughterboard to the optomechanics and fasten it to the daughterboard clamp.

First, the device die was mechanically aligned, glued to the daughterboard to better than 150 μm of its nominal position,[34] and wire bonded. In the second step, light was launched into the OPS. The OPS RBS's were aligned such that the beams went through the microchannel relay and onto the plane where the optoelectronic devices were to be located.

In the third step, the daughterboard was coupled to a six-degree-of-freedom (6-DOF) precision-positioning system and aligned to the optical beams as follows. The daughterboard was adjusted in Δz, θ_x, and θ_y until a traveling microscope setup indicated that these three degrees of freedom were within the desired tolerance. When these three tolerances were achieved, three set screws emerging from holes in the daughterboard clamp (the holes labeled G in Fig. 14) were adjusted such that the set-screw tips just barely touched the front of the board. These three screw tips thus defined the proper plane of the daughterboard relative to the optomechanics. As a result, during the rest of this step the daughterboard never actually touched the clamp, but rather rested and slid on three points approximately 1 mm in front of the clamp. The θ_z accuracy then was verified by use of the imaging system. Finally, the highest contrast ratio of the modulated beams could be used to indicate the optimal x–y alignment of the beams to the device windows.

In the fourth step, after the tolerances in the six degrees of freedom were met, the daughterboard, which was still coupled to the six-degree-of-freedom stage and just barely in contact with the three screw tips, was fastened. The six-degree-of-freedom stage was subsequently decoupled from the daughterboard. This fourth step, namely fastening the aligned daughterboard to the optomechanics, was the most problematic of the entire system-assembly sequence. Two techniques were tried to fasten the board properly; they are described in Subsection 5.B.

B. Daughterboard Fastening Techniques

1. First Daughterboard Fastening Technique: Bolting

In this technique, three additional screws were used. Fastening screws with large heads were inserted into the clearance holes labeled H in Fig. 14 in the daughterboard and screwed into the holes labeled J in the clamp (the diameter of the fastening-screw heads was greater than that of the holes H so that the fastening-screw heads rested against the back side of the board). The fastening screws were then tightened so that the daughterboard did not simply rest on but rather was pressed very hard against the set-screw tips of step three above.

This technique proved to be very cumbersome and had fundamental problems. If the fastening screws were tightened too much, the daughterboard moved during tightening, causing the board to be bolted into an improper position. If, on the other hand, the holding screws were not sufficiently tightened, the board drifted over time. Experimental results indicating the drift are given in Subsection 7.B. Compromising between the two extremes in tightening the screws led to an unsatisfactory result in which the board moved slightly during tightening and drifted slightly afterwards. Consequently, the bolting technique was rejected.

2. Second Daughterboard Fastening Technique: Gluing

In this case, the board was glued to the set-screw tips. After a careful analysis of viscosity, holding force, and ease of curing, a glue from Loctite (No. 403) was chosen. With a syringe, the glue was gently applied to the three set-screw tips, which were just barely touching the daughterboard. This yielded satisfactory results, as the discussion below shows.

6. Mechanical Stability Experiments: Setup

This section describes the diagnostic setup used to measure the effect of mechanical vibrations and shock on the daughterboard x–y (lateral) alignment. Experimental results follow the setup description.

The measurement setup was as follows: In lieu of a smart-pixel die, a quadrant detector (QD) from UDT, Inc.,[35] as shown in Fig. 15, was glued and wire bonded

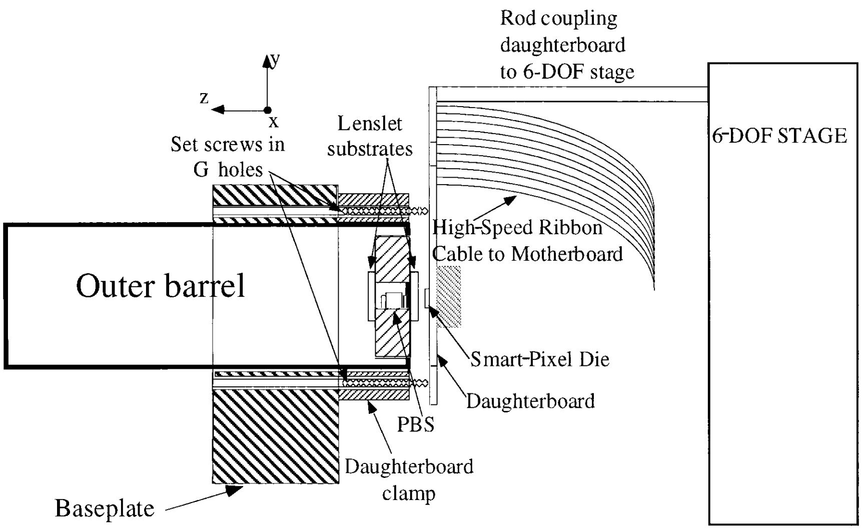

(a)

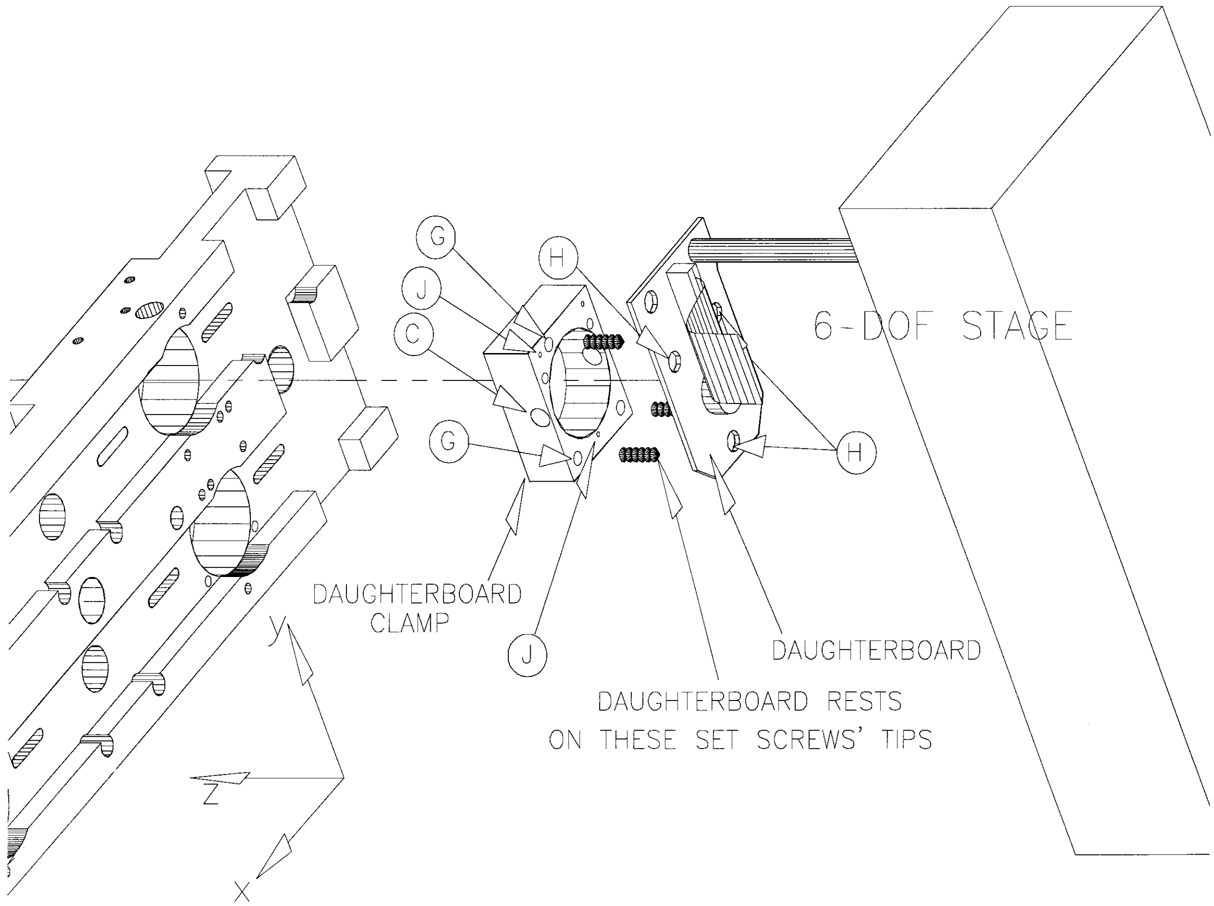

(b)

Fig. 14. (a) Side view of the daughterboard being mounted on the optomechanics. (b) Rear view of the daughterboard being mounted on the optomechanics.

to a daughterboard. Afterwards, one fiber-connected outer-barrel–lenslet–beam-splitter-barrel–OPS assembly, with all the components except the fan-out grating (held by piece 5 in Fig. 1) and the lenslets, was inserted into the baseplate according to the assembly procedure. The daughterboard with the QD was then aligned and fastened to the optomechanics by use of one of the techniques described in Subsections 5.B.1 and 5.B.2.

When light was launched into the OPS (with no

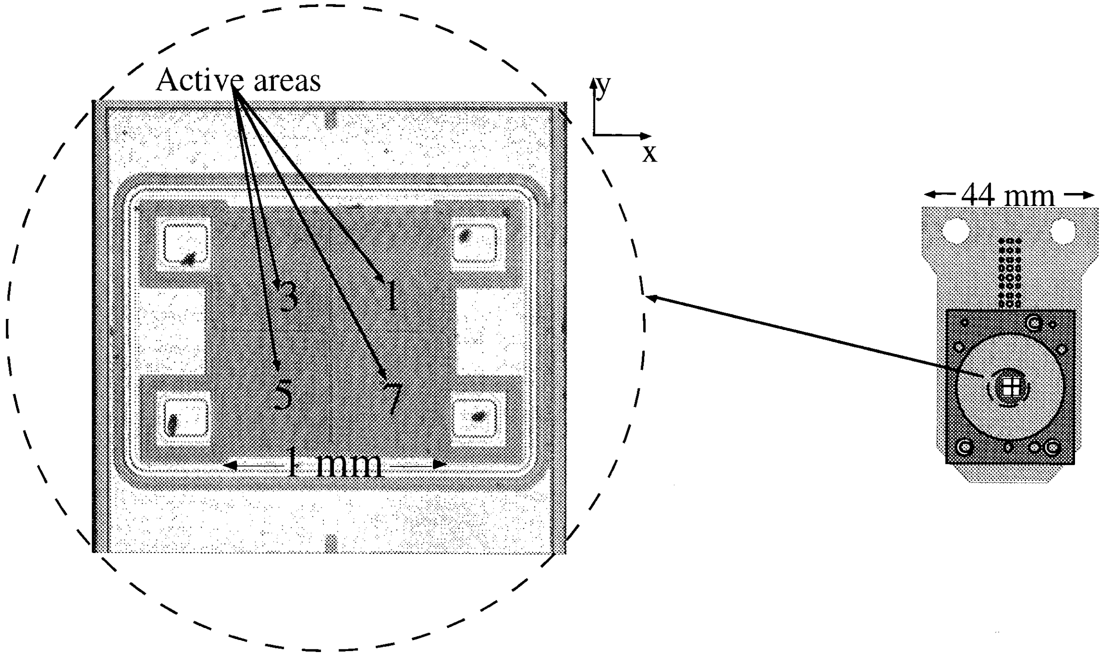

Fig. 15. Quadrant detector mounted on the daughterboard for alignment–diagnostic purposes.

fan-out grating), a single beam went through the OPS and impinged on the QD. At the QD, the beam had a nominal diameter of $3\omega = 1.02$ mm (99% encircled energy). The photocurrents generated by the four photodetectors, labeled 1, 3, 5, and 7 in Fig. 15, of the QD were fed by means of the high-speed ribbon-cable assembly to the dedicated alignment board. On the alignment board, each of the four signals was fed through a low-pass filter having a cutoff frequency of $f_{3dB} = 402$ Hz, buffered, and then finally fed to a Model Lab-NB A/D (analog-digital) board from National Instruments, which sampled each of the four voltages at 4096 samples/s. The low-pass filter was necessary to eliminate aliasing, among other problems associated with frequency. The setup for generating the alignment voltage V_1 is shown in Fig. 16. The three other setups for generating voltages V_3, V_5, and V_7 from their respective quadrants were analogous.

Further processing, such as the calculations required to obtain the Δx and Δy signals from the four sampled voltages, was performed in LABVIEW. For ensuring repeatable results regardless of optical power fluctuations, all misalignment calculations were normalized to the total optical power hitting the detector. For example, from the QD depicted in Fig. 15 it can be seen that

$$\Delta x = k\frac{(V_1 + V_7) - (V_3 + V_5)}{V_1 + V_3 + V_5 + V_7}, \tag{5}$$

where k is a calibration constant, which in this case was obtained experimentally. For this system, the calibration constant was such that the sensitivity was approximately 110 mV/μm for typical power levels. Figure 17 indicates that the system response was linear for a value of $\Delta x < 80$ μm.

7. Mechanical Stability Experiments: Results

The measurement system described in Section 6 was used to characterize many aspects of the optomechanics. This section gives the experimental results obtained.

A. Impact on System Alignment of Fiber Connector Insertion–Extraction

The field serviceability of the fiber-connected power supply was an advantage that this system offered. For this ease of connection to be of greatest use, however, it was imperative that the fiber easily be connected and disconnected without upsetting system alignment. The results of an experiment in which a new fiber with a fiber connector (FC) was connected to and disconnected from the receptacle on the FC bulkhead [part 2 in the assembly drawing (Fig. 1)]

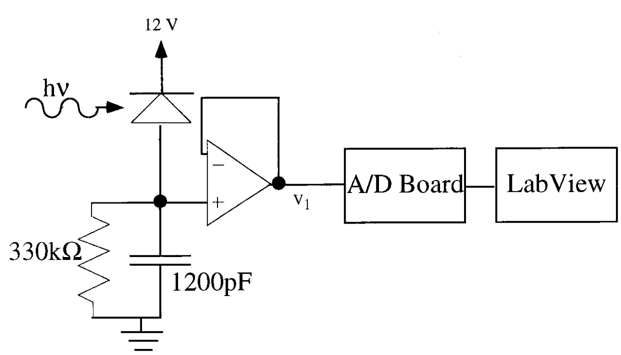

Fig. 16. Electronic setup for generating, buffering, and processing one QD signal.

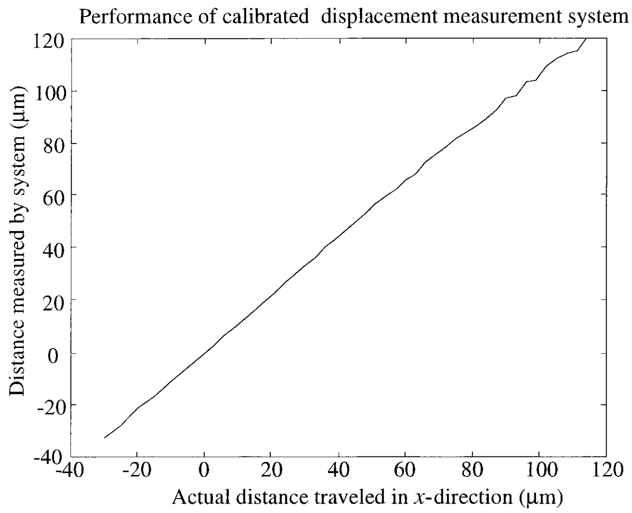

Fig. 17. Calibration and performance of the quadrant detector-based displacement measurement system.

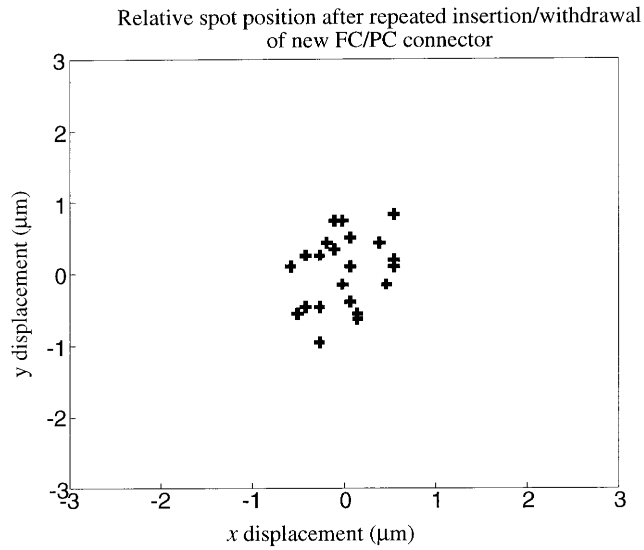

Fig. 18. Effect of repeated insertion–extraction cycles of a FC on the system alignment. Results indicate that inserting–removing the fiber does not affect system alignment to within a ± 1-μm accuracy.

two dozen times within 5 min are shown in Fig. 18. As can be seen, the spot never moved at all, to within the measurement uncertainty of ± 1 μm in this setup. This result is more than simple verification that a single-mode fiber connector has excellent repeatability: It indicates that system alignment was in no way affected either by the small shocks associated with fiber insertion or by the torque imparted to the outer barrel as the connector was hand tightened until the locking screw was snug. However, it should be noted that, if the connector was tightened extremely tightly, the spot did move by approximately 2 or 3 μm. Similar results were obtained for both daughterboard mounting techniques (bolting and gluing).

B. Measurement of Long-Term Drift of the Bolted Daughterboard

This experiment measured the long-term drift of the daughterboard after it was fastened by use of the bolting technique. The bolts were hand tightened sufficiently to hold the board snugly to its mounting clamp on the optomechanics; further tightening of the bolts might have been possible, but repeated experiments indicated that excessive tightening caused the board to move from its aligned position during system assembly.

After the daughterboard was bolted, a large (120 mm $\times$ 120 mm $\times$ 38 mm) industrial cooling fan typical of those mounted in conventional backplane chasses (Model 125DH 1LP11000 from ETRI, Inc.) was bolted to the VME chassis and mounted 50 mm away from the daughterboard. The fan was mounted beside the daughterboard and oriented such that it blew air directly onto the daughterboard. There was considerable clearance around the fan to allow for unimpeded air flow. The fan was fed 500 mA at 12 V dc (according to specifications), which made it rotate at $\sim$3000 rpm (50 Hz). At this frequency, if the flow is unimpeded the fan is specified to blow 102 cfm (cubic feet per minute). The chassis was simply resting on a table and was not clamped down in any manner.

Every day for almost two weeks, with the fan always on at full power, the position of the daughterboard was measured. As can be seen from the results shown in Fig. 19, the daughterboard fell in the y direction by approximately 1 μm/day then stabilized after a week. The repeatability of these measurements was ± 1 μm. As stated above, the poor long-term stability of the daughterboard bolting technique led to its rejection for system assembly.

C. Measurement of the Long-Term Drift of the Glued Daughterboard

This experiment measured the long-term drift of the daughterboard after it was fastened at $(x, y) = (0, 0)$ on day 1 by use of the gluing technique. Measurement results for x and y are shown in Fig. 20.

The most logical interpretation of the long-term drift results shown in Fig. 20 is as follows: The board was glued at (0, 0) ± 2 μm and moved approximately 1 μm during curing. For more than 2 mos after curing the board never moved to within the measurement error, regardless of whether the ETRI 125DH fan in the setup described in Subsection 7.B was blowing air onto the daughterboard. Note that, after the glue had cured, decoupling the daughterboard from the motorized x–y–z stage or extracting–inserting the high-speed ribbon connector on the daughterboard produced no measurable misalignment. The final results are shown in Table 1. Note also that adjusting the RBS's in the OPS can compensate for small errors in x and y. In the case of this long-term drift measurement experiment, measurement repeatability was ± 3 μm.

It should also be noted that, after the glue had cured (which took a few minutes), it left a slight

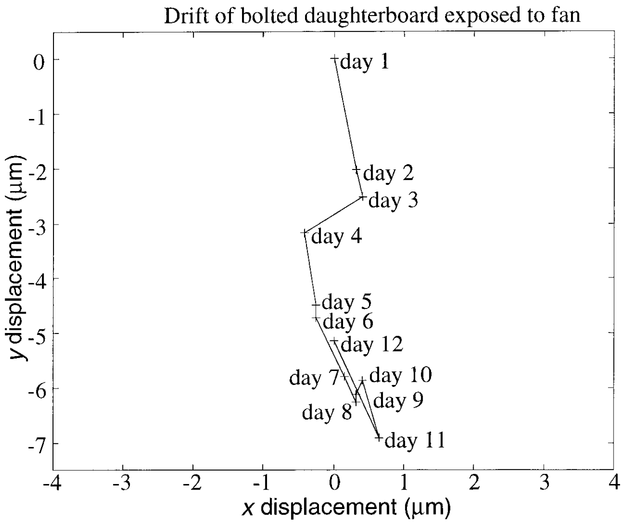

Fig. 19. Drift of a daughterboard fastened by use of the first (bolting) technique.

residue on some of the optics through which the broad alignment beam passed. However, this residue was subsequently measured to be extremely uniform over many millimeters; as a result, this residue had the effect of attenuating by only ~30% the light impinging on the quadrant detector. This attenuation did not affect the measured results since the calculations normalized all power received. A different glue that has no outgassing ("blooming") during curing or a different setup would eliminate this inconvenience.

D. Real-Time Measurements of Mechanical Vibrations of the Glued Daughterboard

Although the glued daughterboard when exposed to the large air currents generated by the fan did not move to within the measurement error over several months, it did exhibit a very interesting behavior when its real-time displacements were analyzed in the spectral domain. For analyzing the spectral behavior of the board's misalignment, fast Fourier transforms of the board's misalignment were performed with LABVIEW.

Figure 21(a) shows the results of the control experiment in which the ETRI Model 125DH fan was turned off. Other than the small spikes at low frequencies (<100 Hz) that are probably due to electrical interference the spectrum was generally quiet.

For the measurements shown in Fig. 21(b), however, the fan was turned on to full power as in previous experiments. In this case, spikes at 410 Hz and at subsequent integer multiples of this fundamental frequency can be discerned for Δx and are readily visible for Δy. The conclusion to be drawn is that the daughterboard mounting system has a mechanical resonance frequency of 410 Hz. This is very encouraging since it is almost an order of magnitude away from most cooling fans' 3000 rpm (50 Hz) rotational frequency; as a result, cooling fans should not cause this system to become mechanically unstable. More sophisticated modeling and measurement techniques obviously would yield more insight; this is a promising route for further research.

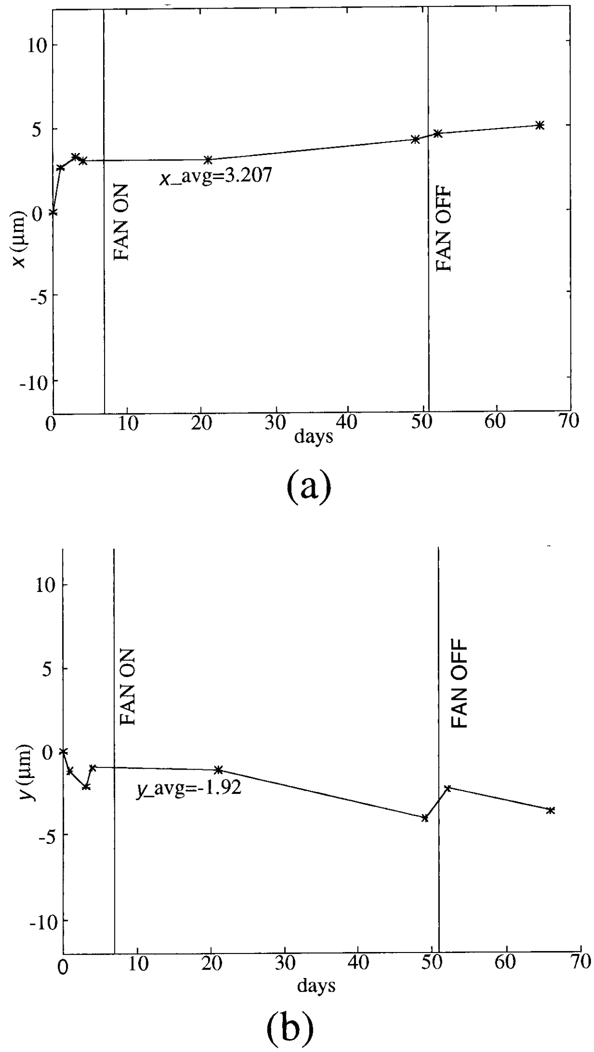

Fig. 20. Long-term drift of a daughterboard fastened by use of glue (second technique) measured across 9 weeks after gluing at day 0: (a) displacement in the x direction and (b) displacement in the y direction.

Even though the low-pass filter at the input-signal source had a half-power cutoff frequency of 402 Hz, the very slow (first-order) roll-off allowed signals in the 800 Hz range to be picked up, albeit with an attenuation of more than 50%.

The vibrations from the fan could have been coupled to the daughterboard in at least two main ways: (1) Since the fan was bolted to the chassis and the daughterboard was glued to the optomechanics, which were also ultimately bolted to the chassis, the fan's mechanical vibrations could have been coupled mechanically from the fan to the daughterboard by means of the chassis and optomechanics, or (2) since the powerful air flow was blowing straight onto the daughterboard and the electrical connector, the air flow itself could have caused the board to vibrate.

Experiments were conducted to determine which of these two alternatives was most responsible for the

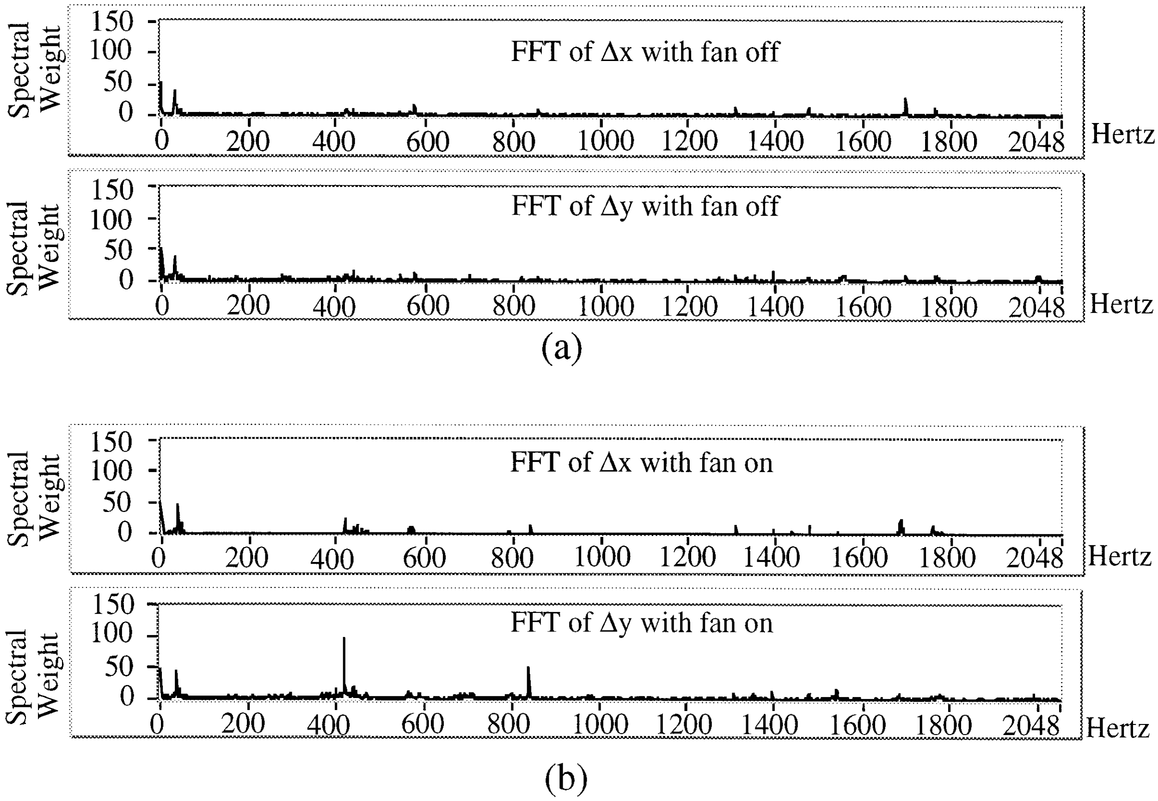

Fig. 21. Spectral behavior of the optomechanical misalignment (a) with the fan off and (b) with the fan on. The number of scans acquired was 4096 at a scanning rate of 4096 scans/s.

daughterboard vibration. In one experiment, the fan was placed in the same position and orientation as before but was attached to the table instead of to the chassis. As a result, the same air flow passed over the board but there was no direct mechanical coupling. In the other experiment, the fan was bolted to the chassis as before, but the air flow to the daughterboard was blocked by a stiff piece of cardboard. The results were inconclusive: Both experiments yielded a spectrum similar to the one shown in Fig. 21(b). More research must be performed in this area.

E. Daughterboard Positioning in Other Degrees of Freedom

The above measurements on daughterboard positioning address only two degrees of freedom: x and y. Of the four remaining degrees of freedom, three were considered critical: the errors in the tilts (θ_x and θ_y) and the error in z_3 (defined in Fig. 4). Given the small size of the array (8×4), a quick visual check before gluing was sufficient to ensure that daughterboard rotation (θ_z) was satisfactory.

With a traveling-microscope arrangement, measuring z_3 was accomplished by measurement of the distance from the edge of the daughterboard to the optomechanics and then subtraction of the known thickness of the die and its glue. Measuring the tilt was accomplished by measurement of z_3 at several positions along the daughterboard edge and use of simple geometrical relations to subtract from these readings a known tilt of the die with respect to the daughterboard. The results are summarized in Table 1.

F. Discussion of Results

The daughterboard mounting technique was labor intensive, and from Table 1 it can be seen that most objectives were probably not met. This is partly due to the extremely tight constraints that were imposed (the target value is for a 1% loss) and partly due to the novelty of the mounting technique, which is quite different from traditional slug-based techniques, given the system constraints. Although the system can still function with the results obtained, a certain number of conclusions can nonetheless be drawn from this work: (1) The interface between optoelectronics and optics is by far the most critical in any system of this nature. (2) A better way of aligning LA_2 to the optoelectronics, either by use of mechanical means or by prealignment of these components to each other before insertion, is necessary. (3) Once assembled, a system like this one is very stable (see Sections 6 and 7).

8. Conclusion

This paper has presented the first, to our knowledge, truly 3-D, vertically oriented, rack-mounted, multistage optomechanical system implementing a free-space optical interconnect. Additionally, the approach chosen can be scaled to much larger systems.

In this paper we have outlined some of the design trade-offs and issues to be faced when designing optomechanics for a free-space digital computing system. It was shown that optical constraints, machining tolerances, optoelectronic technology, electronic packaging, material parameters, thermal effects, and component availability all have a major influence on the optomechanics. Moreover, diagnostic techniques were developed and shown to yield considerable information on the status of the optomechanics. Finally, further avenues of research, such as a better understanding of vibration mechanisms, were proposed.

This research was supported by a grant from the Canadian Institute for Telecommunications Research under the National Centre for Excellence program of Canada and the Nortel/National Sciences and Engineering Research Council (Canada) (NSERC) Chair in Photonic Systems. In addition, D. V. Plant acknowledges support from NSERC (grant OGP0155159) and the Fonds pour la formation de Chercheurs et l'Aide à la Recherche (FCAR) under grant NC-1415. G. Boisset gratefully acknowledges funding from FCAR under grant cttee B2-05.

The lenslets were fabricated by M. Taghizadeh, Department of Physics, Heriot-Watt University (HWU), Edinburgh, Scotland. The authors thank J. Boka and D. Birdie from McGill and G. Smith from HWU for help during fabrication and characterization. The authors also thank the anonymous reviewers for their very helpful and thoughtful comments on the first submission.

References and Notes

1. R. A. Nordin, F. J. Levi, R. N. Nottenburg, J. O'Gorman, T. Tanbun-Ek, and R. A. Logan, "A systems perspective on digital interconnections technology," J. Lightwave Technol. **10,** 811–827 (1992).
2. G. Galilei, *I1 Saggiatore* (Feltrinelli, Milano, Italy, 1656).
3. P. R. Yoder, *Optomechanical Systems Design* (Marcel Dekker, New York, 1993).
4. W. J. Smith, *Modern Optical Engineering: The Design of Optical Systems*, 2nd ed. (McGraw Hill, New York, 1990).
5. D. Vukobratovich, "Advances in optomechanics," in *Applications of Optical Engineering: Proceedings of OE/Midwest '90*, M. K. Dubiel, R. E. Gillespie, R. P. Guzik, and J. E. Pearson, eds., Proc. SPIE **1396,** 436–446 (1990).
6. D. O'Shea, "Annotated bibliography of optomechanical design," Opt. Eng. **25,** 1160–1170 (1986).
7. P. R. Yoder, ed., *Optomechanical Design*, Vol. CR43 of SPIE Critical Reviews Series (SPIE Press, Bellingham, Wash., 1992).
8. F. B. McCormick, T. J. Cloonan, A. L. Lentine, J. M. Sasian, R. L. Morrison, M. G. Beckman, S. L. Walker, M. J. Wojcik, S. J. Hinterlong, R. J. Crisci, R. A. Novotny, and H. S. Hinton, "Five-stage free-space optical switching network with field-effect transistor self-electro-optic-effect-device smart-pixel arrays," Appl. Opt. **33,** 1601–1618 (1994).
9. I. R. Redmond and E. Schenfeld, "A free-space optical interconnection network for massively parallel processing," IEEE LEOS Newsletter **9,** 10–13 (1995).
10. D. V. Plant, B. Robertson, H. S. Hinton, W. M. Robertson, G. C. Boisset, N. H. Kim, Y. S. Liu, M. R. Otazo, D. R. Rolston, and A. Z. Shang, "An optical backplane demonstrator system based on FET-SEED smart pixel arrays and diffractive lenslet arrays," IEEE Photon. Technol. Lett. **7,** 1057–1059 (1995).
11. S. M. Prince, F. A. P. Tooley, S. Wakelin, and M. R. Taghizadeh, "Implementation of optical perfect-shuffle module," Appl. Opt. **34,** 1775–1782 (1995).
12. J. L. Brubaker, F. B. McCormick, F. A. P. Tooley, J. M. Sasian, T. J. Cloonan, A. L. Lentine, S. J. Hinterlong, and M. J. Herron, "Optomechanics of a free-space switch: the components," in *Laser Interferometry IV: Computer-Aided Interferometry*, R. J. Pryputniewicz, ed., Proc. SPIE **1553,** 88–96 (1991).
13. F. B. McCormick, F. A. P. Tooley, J. L. Brubaker, J. M. Sasian, T. J. Cloonan, A. L. Lentine, R. L. Morrison, R. J. Crisci, S. L. Walker, S. J. Hinterlong, and M. J. Herron, "Optomechanics of a free-space photonic switching fabric: the system," in *Optomechanics and Dimensional Stability*, R. A. Paquin and D. Vukobratovich, eds., Proc. SPIE **1533,** 97–114 (1991).
14. J. M. Sasian, F. B. McCormick, R. Webb, R. J. Crisci, K. O. Mersereau, and R. P. Stawicki, "Design, assembly, and testing of an objective lens for a free-space photonic switching system," Opt. Eng. **32,** 1871–1878 (1993).
15. M. Mizukami, K. Koyabu, M. Fukui, and K. Kitayama, "Free-space optical module configuration using a guide-frame assembly method," Appl. Opt. **34,** 1783–1787 (1995).
16. D. R. Rolston, D. V. Plant, T. H. Szymanski, H. S. Hinton, W. S. Hsiao, M. H. Ayliffe, D. Kabal, M. B. Venditti, P. Desai, A. V. Krishnamoorthy, K. W. Goosen, J. A. Walker, B. Tseng, S. P. Hui, J. E. Cunningham, and W. Y. Jan, "A hybrid-SEED smart pixel array for a four-stage intelligent optical backplane demonstrator," IEEE J. Select. Topics Quantum Electron. **2,** 97–105 (1996).
17. IEEE Standard 1014-1987 for a Versatile Backplane Bus: VMEbus, IEEE ref. [1-55937-674-0] [SH11544-NYF] (Institute of Electrical and Electronics Engineers, New York, 1987).
18. D. V. Plant, B. Robertson, H. S. Hinton, M. H. Ayliffe, G. C. Boisset, W. Hsiao, D. Kabal, N. H. Kim, Y. S. Liu, M. R. Otazo, D. Pavlasek, A. Z. Shang, J. Simmons, K. Song, D. A. Thompson, and W. M. Robertson, "A 4 × 4 VCSEL/MSM optical backplane demonstrator system," Appl. Opt. **35,** 6365–6368 (1996).
19. S. Nimmagadda, J. Dillon, and A. Moncayo, "A 533-Mbits/sec/wire modular bus with single or double parallel termination," in *Proceedings of the 1996 Electronic Components and Technology Conference* (Institute of Electrical and Electronics Engineers, New York, 1996), IEEE ref. 0-7803-3286-5/96, pp. 974–983.
20. Lens 322286 (manufactured by the Spindler & Hoyer Corp., Göttingen, Germany).
21. H. S. Hinton, *An Introduction to Photonic Switching Fabrics* (Plenum, New York, 1993).
22. F. B. McCormick, F. A. P. Tooley, T. J. Cloonan, J. M. Sasian, H. S. Hinton, K. O. Mersereau, and A. Y. Feldblum, "Optical interconnections using microlens arrays," Opt. Quantum Electron. **24,** 465–477 (1992).
23. *Metals Handbook* (American Society for Metals, Materials Park, Oh., 1948), pp. 237–243.
24. P. R. Yoder, "Parametric investigation of mounting-induced axial contact stresses in individual lens elements," in *Optomechanical Design*, P. R. Yoder, V. L. Genberg, and D. Vukobratovitch, eds., Proc. SPIE **1998,** 8–19 (1993).
25. R. E. Green, C. J. McCauley, E. Oberg, F. D. Jones, H. L. Horton, and H. H. Ryffel, *Machinery's Handbook*, 25th ed. (Industrial Press, New York, 1996).
26. R. A. Flinn and P. K. Trojan, *Engineering Materials and Their Applications* (Houghton Mifflin, Boston, Mass., 1981).

27. *Properties of Polymer's Engineering Thermoplastics*, Pub. BR/5000-1 5/94 (Polymer Corp., Reading, Pa., 1994).
28. Data sheet 242769-001 (Intel Corp., Santa Clara, Calif., 1995).
29. See, for example, *Design Guide 101 Catalog*, (Nordex Inc., Danbury, Conn., 1991), p. 15A.
30. R. O. Parmley, *Standard Handbook of Fastening and Joining* (McGraw-Hill, New York, 1989), pp. 1–24.
31. H. O'Neill, *Hardness Measurement of Metals and Alloys* (Chapman & Hall, London, 1967), Chap. 2.
32. S. Wakelin, "Design and construction of a free-space digital optical information processor," Ph.D. dissertation (Heriot-Watt University, Edinburgh, Scotland, 1991).
33. R. Iyer, D. J. Goodwill, W. M. Robertson, D. V. Plant, G. C. Boisset, Y. S. Liu, B. Robertson, M. H. Ayliffe, and F. Lacroix, "Design, implementation, and characterization of an optical power supply spot-array generator for a four-stage free-space optical backplane," Appl. Opt. (to be published).
34. D. N. Kabal, G. Boisset, D. R. Rolston, and D. V. Plant, "Packaging of two-dimensional smart pixel arrays," in *Proceedings of the IEEE/LEOS Summer Topical Meeting on Smart Pixels* (IEEE Lasers and Electro-Optical Society, Picataway, N.J., 1996), paper ThA5.
35. Quadrant Detector: Spot 4D M1 [UDT Sensors, Inc. (formerly United Detector Technologies), Hawthorne, Calif., 1997].